EUROPEAN ORGANIZATION FOR NUCLEAR RESEARCH

Leptonic decays of the D_s meson

The ALEPH Collaboration[‡]

Abstract

The purely leptonic decays $D_s \to \tau\nu$ and $D_s \to \mu\nu$ are studied in a sample of four million hadronic Z decays collected with the ALEPH detector at the LEP e^+e^- collider from 1991 to 1995. The branching fractions are extracted from a combination of two analyses, one optimized to select $D_s \to \tau\nu$ decays with $\tau \to e\nu\bar{\nu}$ or $\mu\nu\bar{\nu}$, and the other optimized for $D_s \to \mu\nu$ decays. The results are used to evaluate the D_s decay constant, within the Standard Model: $f_{D_s} = [285 \pm 19(\text{stat}) \pm 40(\text{syst})] \, \text{MeV}$.

Submitted to Physics Letters B

[‡]See the following pages for the list of authors.

The ALEPH Collaboration

A. Heister, S. Schael

Physikalisches Institut das RWTH-Aachen, D-52056 Aachen, Germany

R. Barate, I. De Bonis, D. Decamp, C. Goy, J.-P. Lees, E. Merle, M.-N. Minard, B. Pietrzyk

Laboratoire de Physique des Particules (LAPP), IN^{2}P^3-CNRS, F-74019 Annecy-le-Vieux Cedex, France

G. Boix, S. Bravo, M.P. Casado, M. Chmeissani, J.M. Crespo, E. Fernandez, M. Fernandez-Bosman, Ll. Garrido,[15] E. Graugés, M. Martinez, G. Merino, R. Miquel,[27] Ll.M. Mir,[27] A. Pacheco, H. Ruiz

Institut de Física d'Altes Energies, Universitat Autònoma de Barcelona, E-08193 Bellaterra (Barcelona), Spain[7]

A. Colaleo, D. Creanza, M. de Palma, G. Iaselli, G. Maggi, M. Maggi, S. Nuzzo, A. Ranieri, G. Raso,[23] F. Ruggieri, G. Selvaggi, L. Silvestris, P. Tempesta, A. Tricomi,[3] G. Zito

Dipartimento di Fisica, INFN Sezione di Bari, I-70126 Bari, Italy

X. Huang, J. Lin, Q. Ouyang, T. Wang, Y. Xie, R. Xu, S. Xue, J. Zhang, L. Zhang, W. Zhao

Institute of High Energy Physics, Academia Sinica, Beijing, The People's Republic of China[8]

D. Abbaneo, P. Azzurri, O. Buchmüller,[25] M. Cattaneo, F. Cerutti, B. Clerbaux, H. Drevermann, R.W. Forty, M. Frank, F. Gianotti, T.C. Greening,[29] J.B. Hansen, J. Harvey, D.E. Hutchcroft, P. Janot, B. Jost, M. Kado,[27] P. Mato, A. Moutoussi, F. Ranjard, L. Rolandi, D. Schlatter, O. Schneider,[2] G. Sguazzoni, W. Tejessy, F. Teubert, A. Valassi, I. Videau, J. Ward

European Laboratory for Particle Physics (CERN), CH-1211 Geneva 23, Switzerland

F. Badaud, A. Falvard,[22] P. Gay, P. Henrard, J. Jousset, B. Michel, S. Monteil, J-C. Montret, D. Pallin, P. Perret

Laboratoire de Physique Corpusculaire, Université Blaise Pascal, IN^{2}P^3-CNRS, Clermont-Ferrand, F-63177 Aubière, France

J.D. Hansen, J.R. Hansen, P.H. Hansen, B.S. Nilsson, A. Wäänänen

Niels Bohr Institute, DK-2100 Copenhagen, Denmark[9]

A. Kyriakis, C. Markou, E. Simopoulou, A. Vayaki, K. Zachariadou

Nuclear Research Center Demokritos (NRCD), GR-15310 Attiki, Greece

A. Blondel,[12] G. Bonneaud, J.-C. Brient, A. Rougé, M. Rumpf, M. Swynghedauw, M. Verderi, H. Videau

Laboratoire de Physique Nucléaire et des Hautes Energies, Ecole Polytechnique, IN^{2}P^3-CNRS, F-91128 Palaiseau Cedex, France

V. Ciulli, E. Focardi, G. Parrini

Dipartimento di Fisica, Università di Firenze, INFN Sezione di Firenze, I-50125 Firenze, Italy

A. Antonelli, M. Antonelli, G. Bencivenni, G. Bologna,[4] F. Bossi, P. Campana, G. Capon, V. Chiarella, P. Laurelli, G. Mannocchi,[5] F. Murtas, G.P. Murtas, L. Passalacqua, M. Pepe-Altarelli,[24] P. Spagnolo

Laboratori Nazionali dell'INFN (LNF-INFN), I-00044 Frascati, Italy

A. Halley, J.G. Lynch, P. Negus, V. O'Shea, C. Raine,[4] A.S. Thompson

Department of Physics and Astronomy, University of Glasgow, Glasgow G12 8QQ,United Kingdom[10]

S. Wasserbaech

Department of Physics, Haverford College, Haverford, PA 19041-1392, U.S.A.

R. Cavanaugh, S. Dhamotharan, C. Geweniger, P. Hanke, G. Hansper, V. Hepp, E.E. Kluge, A. Putzer, J. Sommer, H. Stenzel, K. Tittel, S. Werner,[19] M. Wunsch[19]

Kirchhoff-Institut für Physik, Universität Heidelberg, D-69120 Heidelberg, Germany[16]

R. Beuselinck, D.M. Binnie, W. Cameron, P.J. Dornan, M. Girone,[1] N. Marinelli, J.K. Sedgbeer, J.C. Thompson[14]

Department of Physics, Imperial College, London SW7 2BZ, United Kingdom[10]

V.M. Ghete, P. Girtler, E. Kneringer, D. Kuhn, G. Rudolph

Institut für Experimentalphysik, Universität Innsbruck, A-6020 Innsbruck, Austria[18]

E. Bouhova-Thacker, C.K. Bowdery, A.J. Finch, F. Foster, G. Hughes, R.W.L. Jones, M.R. Pearson, N.A. Robertson

Department of Physics, University of Lancaster, Lancaster LA1 4YB, United Kingdom[10]

K. Jakobs, K. Kleinknecht, G. Quast,[6] B. Renk, H.-G. Sander, H. Wachsmuth, C. Zeitnitz

Institut für Physik, Universität Mainz, D-55099 Mainz, Germany[16]

A. Bonissent, J. Carr, P. Coyle, O. Leroy, P. Payre, D. Rousseau, M. Talby

Centre de Physique des Particules, Université de la Méditerranée, IN^{2}P^3-CNRS, F-13288 Marseille, France

F. Ragusa

Dipartimento di Fisica, Università di Milano e INFN Sezione di Milano, I-20133 Milano, Italy

A. David, H. Dietl, G. Ganis,[26] K. Hüttmann, G. Lütjens, C. Mannert, W. Männer, H.-G. Moser, R. Settles, W. Wiedenmann, G. Wolf

Max-Planck-Institut für Physik, Werner-Heisenberg-Institut, D-80805 München, Germany[16]

J. Boucrot, O. Callot, M. Davier, L. Duflot, J.-F. Grivaz, Ph. Heusse, A. Jacholkowska, J. Lefrançois, J.-J. Veillet, C. Yuan

Laboratoire de l'Accélérateur Linéaire, Université de Paris-Sud, IN^{2}P^3-CNRS, F-91898 Orsay Cedex, France

G. Bagliesi, T. Boccali, L. Foà, A. Giammanco, A. Giassi, F. Ligabue, A. Messineo, F. Palla, G. Sanguinetti, A. Sciabà, R. Tenchini,[1] A. Venturi,[1] P.G. Verdini

Dipartimento di Fisica dell'Università, INFN Sezione di Pisa, e Scuola Normale Superiore, I-56010 Pisa, Italy

G.A. Blair, G. Cowan, M.G. Green, T. Medcalf, A. Misiejuk, J.A. Strong, P. Teixeira-Dias, J.H. von Wimmersperg-Toeller

Department of Physics, Royal Holloway & Bedford New College, University of London, Egham, Surrey TW20 OEX, United Kingdom[10]

R.W. Clifft, T.R. Edgecock, P.R. Norton, I.R. Tomalin

Particle Physics Dept., Rutherford Appleton Laboratory, Chilton, Didcot, Oxon OX11 OQX, United Kingdom[10]

B. Bloch-Devaux, P. Colas, S. Emery, W. Kozanecki, E. Lançon, M.-C. Lemaire, E. Locci, P. Perez, J. Rander, J.-F. Renardy, A. Roussarie, J.-P. Schuller, J. Schwindling, A. Trabelsi,[21] B. Vallage

CEA, DAPNIA/Service de Physique des Particules, CE-Saclay, F-91191 Gif-sur-Yvette Cedex, France[17]

N. Konstantinidis, A.M. Litke, G. Taylor

Institute for Particle Physics, University of California at Santa Cruz, Santa Cruz, CA 95064, USA[13]

C.N. Booth, S. Cartwright, F. Combley,[4] M. Lehto, L.F. Thompson

Department of Physics, University of Sheffield, Sheffield S3 7RH, United Kingdom[10]

K. Affholderbach,[28] A. Böhrer, S. Brandt, C. Grupen, A. Ngac, G. Prange, U. Sieler

Fachbereich Physik, Universität Siegen, D-57068 Siegen, Germany[16]

G. Giannini

Dipartimento di Fisica, Università di Trieste e INFN Sezione di Trieste, I-34127 Trieste, Italy

H. He, J. Putz, J. Rothberg

Experimental Elementary Particle Physics, University of Washington, Seattle, WA 98195 U.S.A.

S.R. Armstrong, K. Berkelman, K. Cranmer, D.P.S. Ferguson, Y. Gao,[20] S. González, O.J. Hayes, H. Hu, S. Jin, J. Kile, P.A. McNamara III, J. Nielsen, Y.B. Pan, J.H. von Wimmersperg-Toeller, W. Wiedenmann, J. Wu, Sau Lan Wu, X. Wu, G. Zobernig

Department of Physics, University of Wisconsin, Madison, WI 53706, USA[11]

G. Dissertori

Institute for Particle Physics, ETH Hönggerberg, 8093 Zürich, Switzerland.

1 Introduction

The leptonic decays of the D_s meson are interesting because they open a window onto the strong interactions of the constituent quarks of the D_s. The absence of strong interactions among the final state particles makes the interpretation of the measurements particularly straightforward. The information gained is useful in understanding other processes involving heavy pseudoscalar mesons.

The decay $D_s \to l\nu$ is the second-generation analogue of charged pion decay, $\pi^+ \to l\nu$. The $D_s \to l\nu$ decay proceeds via the Cabibbo allowed annihilation of the c and $\bar{s}$ quarks in the D_s; the rate depends on the c$\bar{s}$ wavefunction at zero separation[1]. The annihilation amplitude is characterized by the D_s decay constant f_{D_s}, defined as

$$i f_{D_s} p_\mu^{(D_s)} = \langle D_s | \bar{c} \gamma_\mu \gamma_5 s | 0 \rangle \ . \tag{1}$$

In the Standard Model the leptonic branching fraction is then given by

$$B(D_s \to l\nu) = \frac{G_F^2}{8\pi} \tau_{D_s} f_{D_s}^2 |V_{cs}|^2 m_{D_s} m_l^2 \left(1 - \frac{m_l^2}{m_{D_s}^2} \right)^2 , \tag{2}$$

where τ_{D_s} is the mean lifetime of the D_s, V_{cs} is the relevant CKM matrix element, m_{D_s} is the mass of the D_s, and m_l is the mass of the lepton.

It is worthwhile to measure f_{D_s} because it characterizes the structure of the D_s meson and can be calculated in various theoretical models. Lattice QCD is now generally considered to be the most reliable method for calculating the pseudoscalar meson decay constants; recent results yield a prediction of $f_{D_s} = 255 \pm 30 \, \text{MeV}$ [1]. An important application of the lattice QCD calculations of decay constants is in the evaluation of the third-generation Cabibbo-Kobayashi-Maskawa matrix elements. Constraints on these elements are obtained from measurements of B^0-$\bar{B}^0$ mixing and rely on theoretical estimates of f_B, which is experimentally inaccessible at present. A measurement of f_{D_s} therefore serves as a useful check of the theoretical methods.

The relative branching fractions for $D_s \to e\nu$, $\mu\nu$, and $\tau\nu$ are known precisely in the Standard Model. From Eq. 2, the ratios of branching fractions are $B(D_s \to e\nu)/B(D_s \to \tau\nu) = 2.5 \times 10^{-6}$ and $B(D_s \to \mu\nu)/B(D_s \to \tau\nu) = 0.103$. The helicity suppression in these decays leads to an extremely small branching fraction for the electron mode. An investigation of the muon and tau modes is presented in this paper.

The helicity suppression is lifted if a photon is radiated from one of the quarks, giving $D_s \to \gamma l\nu$. The analysis of Ref. [2] leads to an estimate of the ratio $r = B(D_s \to \gamma\mu\nu)/B(D_s \to \mu\nu) \cong 0.014$ to 0.11 with $B(D_s \to \gamma e\nu) \cong B(D_s \to \gamma\mu\nu)$. The prediction in [3] is smaller, $r \cong 0.0059$. In either case, the effect of $D_s \to \gamma l\nu$ decays on the present investigation would be small or negligible, and no correction is made for these decays.

The data sample and detector are briefly described in Section 2. Two analyses are then presented, one optimized to select $D_s \to \tau\nu$ decays (Section 3) and one optimized to select $D_s \to \mu\nu$ decays (Section 4). The systematic errors are discussed in Section 5, and the combined results and conclusions are given in Section 6.

---

[1] Charge-conjugate states are implied throughout this paper.

2   Data sample and apparatus

The analyses are based on a data sample collected with the ALEPH detector at the LEP e^+e^- collider in 1991 through 1995, at or near the peak of the Z resonance. The sample corresponds to 3.97×10^6 produced $e^+e^- \rightarrow q\bar{q}$ events.

Detailed descriptions of the ALEPH detector and its performance may be found in [4–6]. The tracking system consists of a high-resolution silicon strip vertex detector (VDET), a cylindrical drift chamber (the inner tracking chamber or ITC), and a large time projection chamber (TPC). The VDET comprises two layers of double-sided silicon strip detectors at average radii of 6.3 and 10.8 cm. The spatial resolution for the r-ϕ and z projections (transverse to and along the beam axis, respectively) is $12\,\mu$m at normal incidence. The angular coverage is $|\cos\theta| < 0.85$ for the inner layer and $|\cos\theta| < 0.69$ for the outer layer. The ITC has eight coaxial wire layers at radii from 16 to 26 cm. The TPC provides up to 21 three-dimensional coordinates per track at radii between 40 and 171 cm, as well as measurements of the specific ionization energy loss (dE/dx) of charged particles. The tracking detectors are contained within a superconducting solenoid, which produces an axial magnetic field of 1.5 T. Charged tracks measured in the VDET-ITC-TPC system are reconstructed with a momentum resolution of $\Delta p/p = 6 \times 10^{-4}\, p_t \oplus 0.005$ (p_t in GeV/c). An impact parameter resolution of $22\,\mu$m in the r-ϕ plane is achieved for muons from $Z \rightarrow \mu^+\mu^-$ having at least one VDET r-ϕ hit. These performance figures reflect the improvements obtained from the 1998 reprocessing of the ALEPH LEP1 data set with enhanced event reconstruction algorithms [7].

Surrounding the TPC is an electromagnetic calorimeter (ECAL), a lead/wire-chamber sandwich operated in proportional mode. The calorimeter is read out via projective towers subtending typically $0.9° \times 0.9°$ which sum the deposited energy in three sections in depth. Beyond the ECAL lies the solenoid, followed by a hadron calorimeter (HCAL), which uses the iron return yoke as absorber and has an average depth of 1.50 m. Hadronic showers are sampled by 23 planes of streamer tubes, providing a digital hit pattern and inducing an analog signal on pads arranged in projective towers. The HCAL is used in combination with two layers of muon chambers outside the magnet for μ identification.

The measurements of charged particle momenta and of energy depositions in the calorimeters, combined with the identification of photons, electrons, and muons, are used to produce a list of charged and neutral *energy flow particles* in each event [6].

3 $D_s \rightarrow \tau\nu$ analysis

The first analysis [8] is designed to search for the decay chain $e^+e^- \rightarrow c\bar{c}$, $c \rightarrow D_s \rightarrow \tau\nu$, with $\tau \rightarrow e\nu\bar{\nu}$ or $\tau \rightarrow \mu\nu\bar{\nu}$. The electron and muon channels are treated separately. As the final state under study contains three neutrinos, the signature of these decays is an identified lepton and large missing energy in one hemisphere of the event.

Although the $e^+e^- \rightarrow b\bar{b}$ event sample contains more D_s mesons than the $c\bar{c}$ sample, the $D_s \rightarrow l\nu$ signal is more difficult to isolate in $b\bar{b}$ events due to the softer D_s spectrum and the large number of semileptonic b decays. Cuts are therefore applied to remove $b\bar{b}$ events, and the analyses are optimized to select D_s decays in $c\bar{c}$ events.

3.1 Event selection

Hadronic Z decays are preselected using charged tracks [9]. Backgrounds from two-photon interactions and dilepton events are reduced to a negligible level by means of additional cuts on the numbers of reconstructed charged and neutral particles. The event thrust axis is required to satisfy $|\cos\theta_{\mathrm{thrust}}| < 0.8$ to select events within the acceptance of the vertex detector. Each event is then separated into two hemispheres by the plane perpendicular to the thrust axis. The total energy of each hemisphere is calculated and the hemisphere with larger missing energy is selected if it contains an identified lepton (e or μ). Electron identification is based on the shower shape in the electromagnetic calorimeter and the ionization in the time projection chamber; muon identification makes use of the digital pattern information in the hadron calorimeter and hits in the muon chambers [10]. If more than one lepton is present in the selected hemisphere, the one with the highest momentum is considered. The missing energy in the hemisphere is required to be greater than $5\,\mathrm{GeV}$ to reduce the background. The hemisphere invariant masses are taken into account in the calculation of the expected hemisphere energies [11].

To further reduce the background from $\mathrm{b\bar{b}}$ events, cuts are applied to a set of hemisphere variables based on the pseudorapidities and impact parameters of the charged tracks. The energy flow particles are clustered into jets by means of the JADE algorithm with $y_{\mathrm{cut}} = 0.003$. The pseudorapidity η of a particle is then defined as $\eta = -\ln\tan(\alpha/2)$, where α is the laboratory angle between the particle and the nearest jet axis. The reconstructed particles in $\mathrm{c\bar{c}}$ events tend to have larger pseudorapidities than those in $\mathrm{b\bar{b}}$ events because of the lower mass of c hadrons compared to b hadrons. An existing ALEPH lifetime-based b tag algorithm [12] was modified to include a dependence on the pseudorapidity of the charged tracks. The tracks in each hemisphere are divided into two groups, one with $\eta \geq 5.1$ and one with $\eta < 5.1$. For each group, the confidence level for the hypothesis that all tracks originate from the Z production point is then calculated. The selected lepton track is not included in this calculation. To reject $\mathrm{b\bar{b}}$ events, a cut is made on the confidence level for the low-η group in each hemisphere. A further rejection of $\mathrm{c\bar{c}}$ background events[2] is obtained by cutting on the confidence level for the high-η group in the hemisphere containing the lepton; with the lepton excluded, signal events have only fragmentation tracks in the lepton hemisphere and can be distinguished from $\mathrm{c\bar{c}}$ background events.

The momentum and energy of the $\mathrm{D_s}$ candidate are reconstructed from the observed charged and neutral particles in the event by excluding the lepton l and applying four-momentum conservation:

$$\vec{P}_{\mathrm{D_s}} = -\sum_{i\neq l}\vec{P}_i$$
$$E_{\mathrm{D_s}} = \sqrt{s} - \sum_{i\neq l}E_i \; .$$

This procedure is based on the assumption that no neutrinos are produced in the hemisphere opposite the $\mathrm{D_s}$ candidate. A kinematic fit is performed in which the energies of all reconstructed particles (except the lepton) are varied such that the constraint

---

[2]Throughout this paper, light quark-antiquark (denoted "uds"), $\mathrm{c\bar{c}}$, and $\mathrm{b\bar{b}}$ background events are defined to be those events containing no $\mathrm{D_s} \rightarrow l\nu$ or $\mathrm{D^+} \rightarrow l\nu$ decays.

$[E_{D_s}^2 - P_{D_s}^2 c^2]^{1/2} = M_{D_s} c^2 = 1.968$ GeV is satisfied. The energy resolutions for charged, neutral electromagnetic, and neutral hadronic particles are parametrized from simulated events. The kinematic fit improves the energy resolution of D_s candidates from 6.7 GeV to 3.5 GeV. The background is further reduced by the requirement that the fitted D_s energy be greater than 22.5 GeV. The selection efficiency for $c\bar{c} \to D_s \to \tau\nu$ events is 2.5% (3.3%) in the electron (muon) channel [including the factor of $B(\tau \to l\nu\bar{\nu})$]. This procedure selects 3956 and 6637 events in the electron and muon channels, respectively.

3.2 Linear discriminant analysis

A linear discriminant analysis is performed on Monte Carlo events to search for an optimal linear combination of event variables so that maximum discrimination between signal and background is achieved. Two discriminating variables, U_c and U_b, are created to distinguish the $c\bar{c} \to D_s \to \tau\nu$ signal events from $c\bar{c}$ and $b\bar{b}$ backgrounds, respectively; the backgrounds arise mainly from semileptonic c and b decays. Nine variables are selected to form U_c and ten for U_b. The variables with the greatest discrimination power include the fitted D_s momentum, the angle between the lepton and the D_s direction in the D_s rest frame, several b tag variables, and the lepton transverse momentum with respect to the nearest jet axis. The definitions of U_c and U_b are optimized independently in the electron and muon channels. The distributions of U_b versus U_c are shown in Figs. 1 and 2.

The branching fraction $B(D_s \to \tau\nu)$ is extracted from a maximum likelihood fit to the unbinned U_b versus U_c distribution in each channel. The two-dimensional fitting function consists of one signal and three background (uds, $c\bar{c}$, and $b\bar{b}$) components. Although the analysis is optimized to select $D_s \to \tau\nu$ decays, some $D_s \to \mu\nu$ decays are also accepted. Because these two decay rates are both proportional to $f_{D_s}^2$, both types of decays are considered to be part of the signal in the fit to the data. Leptonic D^+ decays also pass the selection and are included in the signal. The production of D_s and D^+ mesons in the remaining $b\bar{b}$ events must be taken into account as well. The signal component of the fitting function is therefore taken to be the combination of D_s and D^+ decays to $\tau\nu$ and $\mu\nu$ in $c\bar{c}$ and $b\bar{b}$ events. The relative normalizations of these eight contributions are fixed according to Eq. 2 and the measured charm production rates [13, 14]; $f_{D_s}/f_D = 1.11^{+0.06}_{-0.05}$ from lattice QCD calculations [15]; R_c and R_b from the Standard Model fit in [13]; $|V_{cs}|$ and $|V_{cd}|$ from [16]; the D_s and D^+ lifetimes from [16]; and particle masses from [16]. The normalizations are shown in Table 1. Leptonic D^+ decays are Cabibbo suppressed and contribute less than 8% of the total signal. Each component of the fitting function is parametrized as the sum of up to five two-dimensional correlated Gaussian functions from a fit to simulated events.

A program based on `JETSET` 7.4 [17] and tuned to ALEPH data [18] was used to generate the Monte Carlo sample of 15 million $e^+e^- \to q\bar{q}$ background events (including 3.7 million $c\bar{c}$ and 6.6 million $b\bar{b}$ events) and 370 000 events containing D_s and D^+ leptonic decays. The polarization of the τ is taken into account in the simulation of (pseudoscalar) $\to \tau\nu$ decays.

The free parameters in the fit to the data are the numbers of events in the signal and the three background components. The fitting procedure is tested with Monte Carlo events to be free of bias.

ALEPH

Figure 1: Monte Carlo U_b versus U_c distributions in the electron channel of the $\tau\nu$ analysis, after all cuts: (a) signal, $c\bar{c} \to D_s \to \tau\nu$; (b) uds background; (c) $c\bar{c}$ background; (d) $b\bar{b}$ background. The area of the square in each bin is proportional to the number of entries. The distributions are shown with arbitrary normalizations.

5

ALEPH

(a) Signal: $c\bar{c} \to D_s \to \tau\nu$

(b) Background: uds events

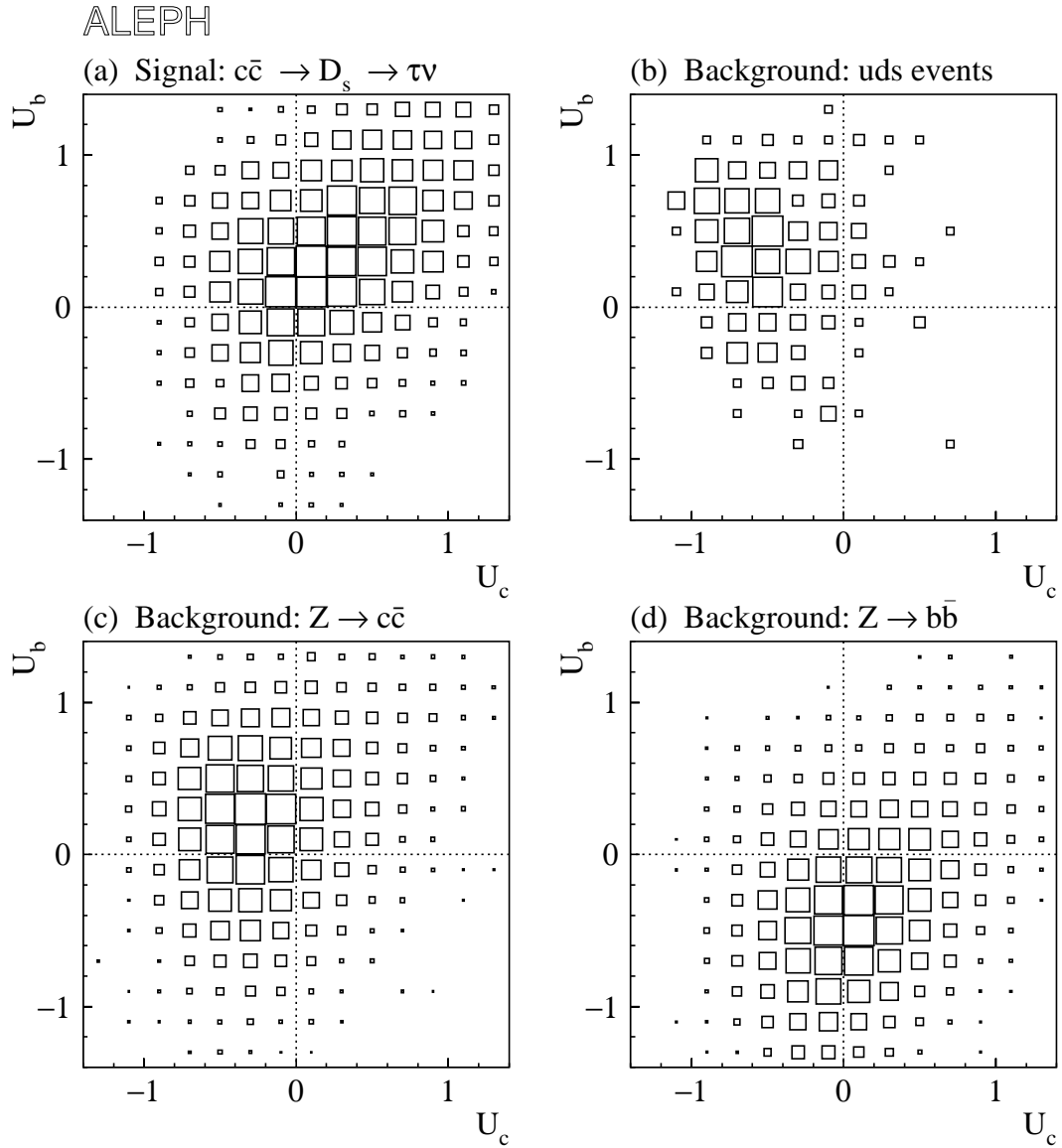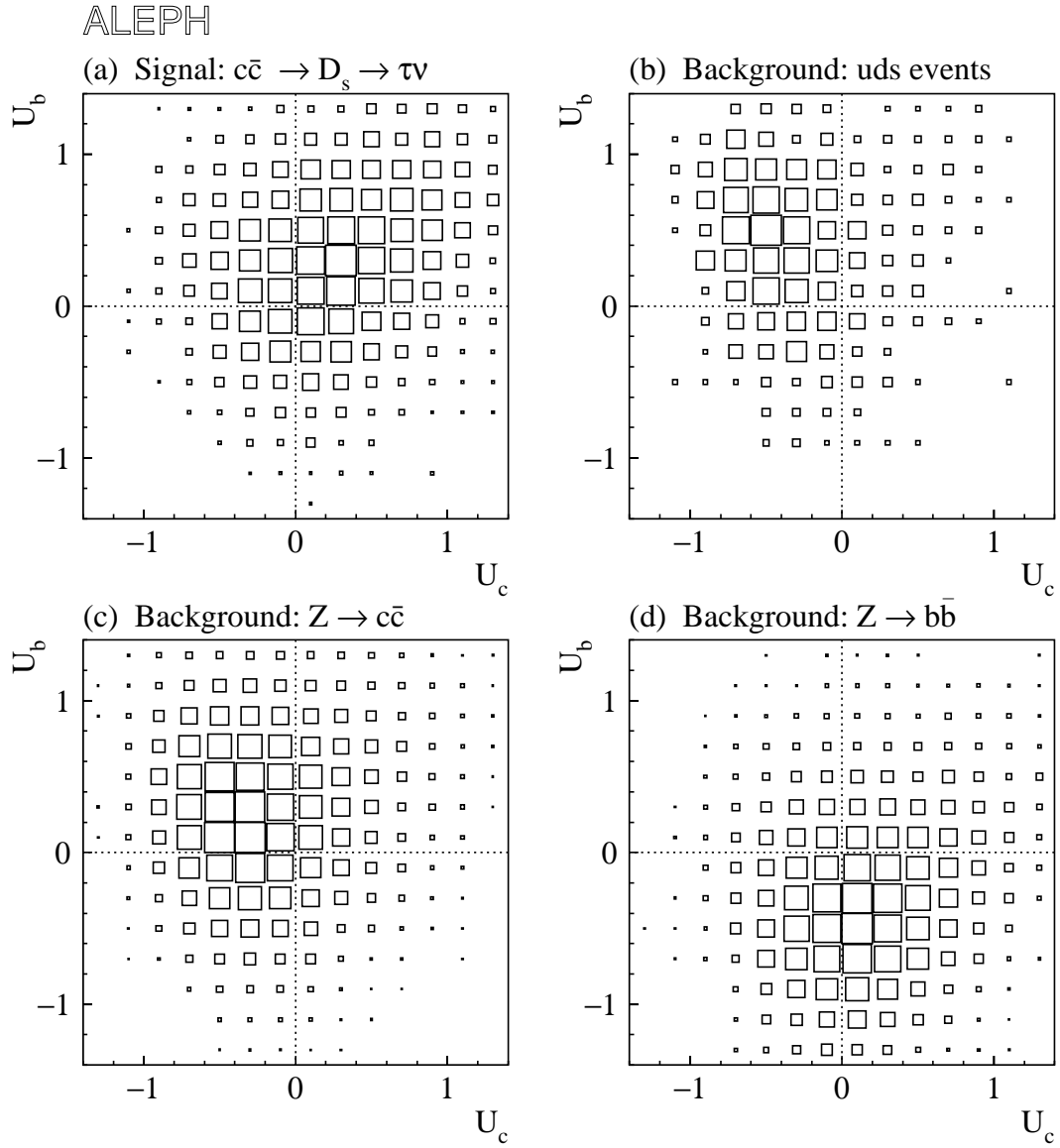**(c) Background: $Z \to c\bar{c}$**

(d) Background: $Z \to b\bar{b}$

Figure 2: Monte Carlo U_b versus U_c distributions in the muon channel of the $\tau\nu$ analysis, after all cuts: (a) signal, $c\bar{c} \to D_s \to \tau\nu$; (b) uds background; (c) $c\bar{c}$ background; (d) $b\bar{b}$ background. The distributions are shown with arbitrary normalizations.

Table 1: Relative normalizations of the contributions to the signal in the $\mathrm{D_s} \to \tau\nu$ analysis.

	Fraction of signal (%)	
Source	e channel	μ channel
$\mathrm{c\bar{c}} \to \mathrm{D_s} \to \tau\nu$	76.9	52.4
$\mathrm{c\bar{c}} \to \mathrm{D_s} \to \mu\nu$	0.5	26.4
$\mathrm{b\bar{b}} \to \mathrm{D_s} \to \tau\nu$	17.4	10.7
$\mathrm{b\bar{b}} \to \mathrm{D_s} \to \mu\nu$	1.2	3.1
$\mathrm{c\bar{c}} \to \mathrm{D^+} \to \tau\nu$	3.4	2.3
$\mathrm{c\bar{c}} \to \mathrm{D^+} \to \mu\nu$	0.1	4.4
$\mathrm{b\bar{b}} \to \mathrm{D^+} \to \tau\nu$	0.4	0.4
$\mathrm{b\bar{b}} \to \mathrm{D^+} \to \mu\nu$	0.2	0.4
Total	100.0	100.0

Table 2: Fitted numbers of signal and background events in data in the $\mathrm{D_s} \to \tau\nu$ analysis. Only the statistical uncertainties from the fit are shown.

Component	e channel	μ channel
Signal	306 ± 62	575 ± 84
uds background	111 ± 56	455 ± 139
$\mathrm{c\bar{c}}$ background	2310 ± 101	3750 ± 182
$\mathrm{b\bar{b}}$ background	1228 ± 56	1857 ± 74

3.3 Results

The projections of the two-dimensional fits to the data are shown in Figs. 3 and 4. The fitted numbers of signal and background events are listed in Table 2. The fitted branching fractions from the electron and muon channels are $B(\mathrm{D_s} \to \tau\nu) = [5.86 \pm 1.18(\text{stat})]\%$ and $[5.78 \pm 0.85(\text{stat})]\%$, respectively.

The goodness of fit is evaluated by comparing the likelihood value obtained from each fit to the data with the distribution of likelihoods obtained from fits to many toy Monte Carlo samples. The fitting functions are used to define the parent distributions in generating these samples. The fit confidence levels are calculated to be 83% in the electron channel and 81% in the muon channel; the $\mathrm{U_b}$ versus $\mathrm{U_c}$ distributions in the data are well described by the fitting functions. The same projections are also shown in Figs. 3 and 4 after subtraction of the fitted background components. The distribution of the excess events is consistent in shape with the Monte Carlo prediction for the signal.

It is desirable to visualize the results of the two-dimensional fits in one-dimensional distributions. For this purpose, the purity P of each event is calculated. The purity of event i is defined as

$$P_i = \frac{S(\mathrm{U_c^{(i)}}, \mathrm{U_b^{(i)}})}{S(\mathrm{U_c^{(i)}}, \mathrm{U_b^{(i)}}) + B(\mathrm{U_c^{(i)}}, \mathrm{U_b^{(i)}})} \; ,$$

where $\mathrm{U_c^{(i)}}$ and $\mathrm{U_b^{(i)}}$ are the values of the discriminant variables for event i, and S and

Figure 3: Projections of the fit to the data in the electron channel of the $D_s \rightarrow \tau\nu$ analysis: (a) U_c distribution; (b) U_b distribution. The data are shown by the squares with error bars. The solid curves are the fitted distributions, while the dashed curves show the signal contributions. The same distributions are shown in (c) and (d), after subtraction of the fitted backgrounds.
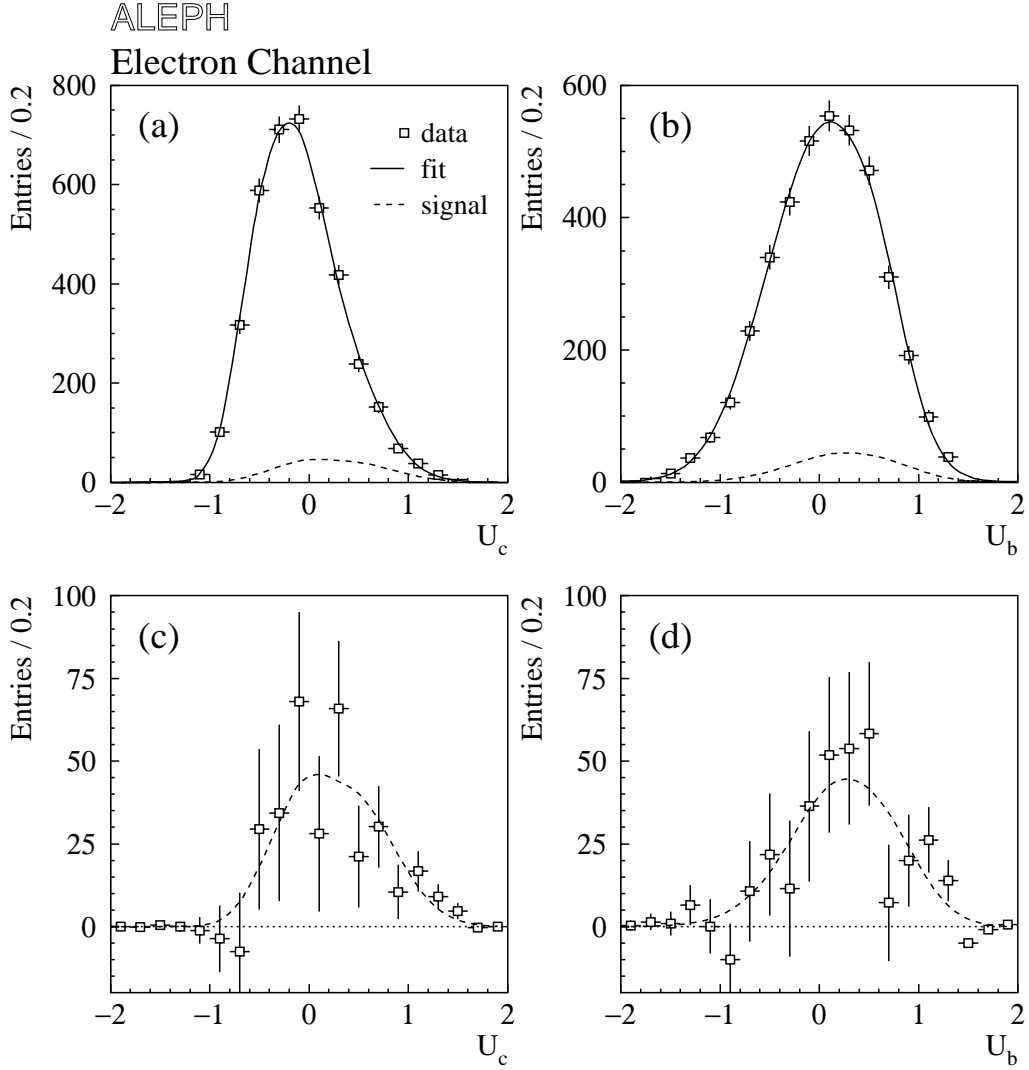
Figure 4: Projections of the fit to the data in the muon channel of the $D_s \rightarrow \tau\nu$ analysis: (a) U_c distribution; (b) U_b distribution. The data are shown by the squares with error bars. The solid curves are the fitted distributions, while the dashed curves show the signal contributions. The same distributions are shown in (c) and (d), after subtraction of the fitted backgrounds.
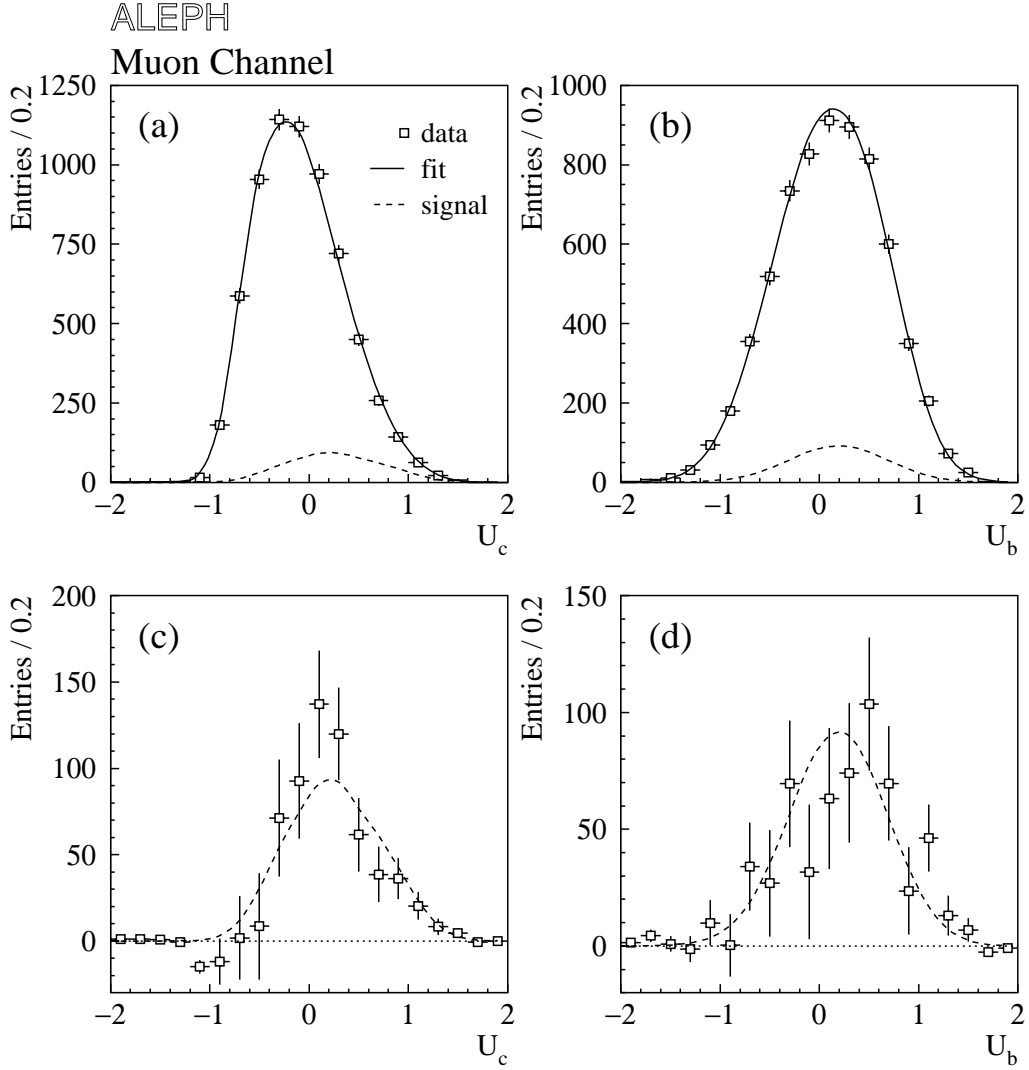
9

B represent the distributions of the signal and background, normalized according to the results of the fit. The distributions of P are quite different for signal and background events. The purity distributions from the electron and muon channels are shown in Figs. 5a and b; the background-subtracted distributions are given in Figs. 5c and d. These figures show that the shapes of the observed purity distributions agree with the expectations. In particular, the shape of the data distribution in each channel after background subtraction is consistent with the simulated signal and inconsistent with the simulated background.

4 $\mathrm{D_s} \rightarrow \mu\nu$ analysis

The second analysis [19] is optimized to select $\mathrm{e^+e^-} \rightarrow \mathrm{c\bar{c}}$ events containing the decay $\mathrm{D_s} \rightarrow \mu\nu$.

4.1   Event selection

The same preselection of hadronic Z decays is performed as in the $\tau\nu$ analysis. A cut on the number of reconstructed charged tracks coming from the area of the interaction point is applied to reduce the background from dilepton events. The event thrust axis is required to satisfy $|\cos\theta_{\mathrm{thrust}}| < 0.8$. A loose muon identification algorithm [19], requiring either muon chamber hits or a muon-like digital pattern in the HCAL, is used to select muon candidates. If more than one muon is present in the event, the one with highest momentum is selected.

A kinematic fit is then performed in order to improve the resolution on the missing momentum, assumed to arise from the undetected neutrino from $\mathrm{D_s} \rightarrow \mu\nu$. In this fit, the missing mass is constrained to be zero and the $\mathrm{D_s}$ displacement direction (from the event primary vertex to the $\mathrm{D_s}$ decay vertex, i.e., an unknown point on the muon track) is constrained to be parallel to the $\mathrm{D_s}$ momentum direction. This constraint is equivalent to requiring that the reconstructed neutrino direction be parallel to a plane containing the primary vertex and the muon track. The energies of the reconstructed charged and neutral particles are varied in the fit, while their directions are held constant. The muon track impact parameters and the coordinates of the event primary vertex are also allowed to vary within their uncertainties. The kinematic fit improves the resolution on the neutrino energy from $5.7\,\mathrm{GeV}$ to $2.8\,\mathrm{GeV}$ and on the neutrino direction from $8.9°$ to $6.2°$.

The $\mathrm{b\bar{b}}$ background and some of the $\mathrm{c\bar{c}}$ background are further reduced by cuts on the track pseudorapidities and impact parameters, as described in Section 3.1. Finally, a hard cut is made on the fitted energy of the $\mathrm{D_s}$ candidate, $E_\mu + E_\nu > 28\,\mathrm{GeV}$. This procedure selects 7164 events in the data.

4.2   Linear discriminant analysis

Linear discriminant variables $\mathrm{U_c}$ and $\mathrm{U_b}$ are optimized to distinguish $\mathrm{c\bar{c}} \rightarrow \mathrm{D_s} \rightarrow \mu\nu$ signal events from $\mathrm{c\bar{c}}$ and $\mathrm{b\bar{b}}$ backgrounds, respectively. Each of the linear discriminant variables is a combination of seven event variables. The variables with the greatest discrimination power include the muon momentum, the fitted neutrino momentum, and several b- and
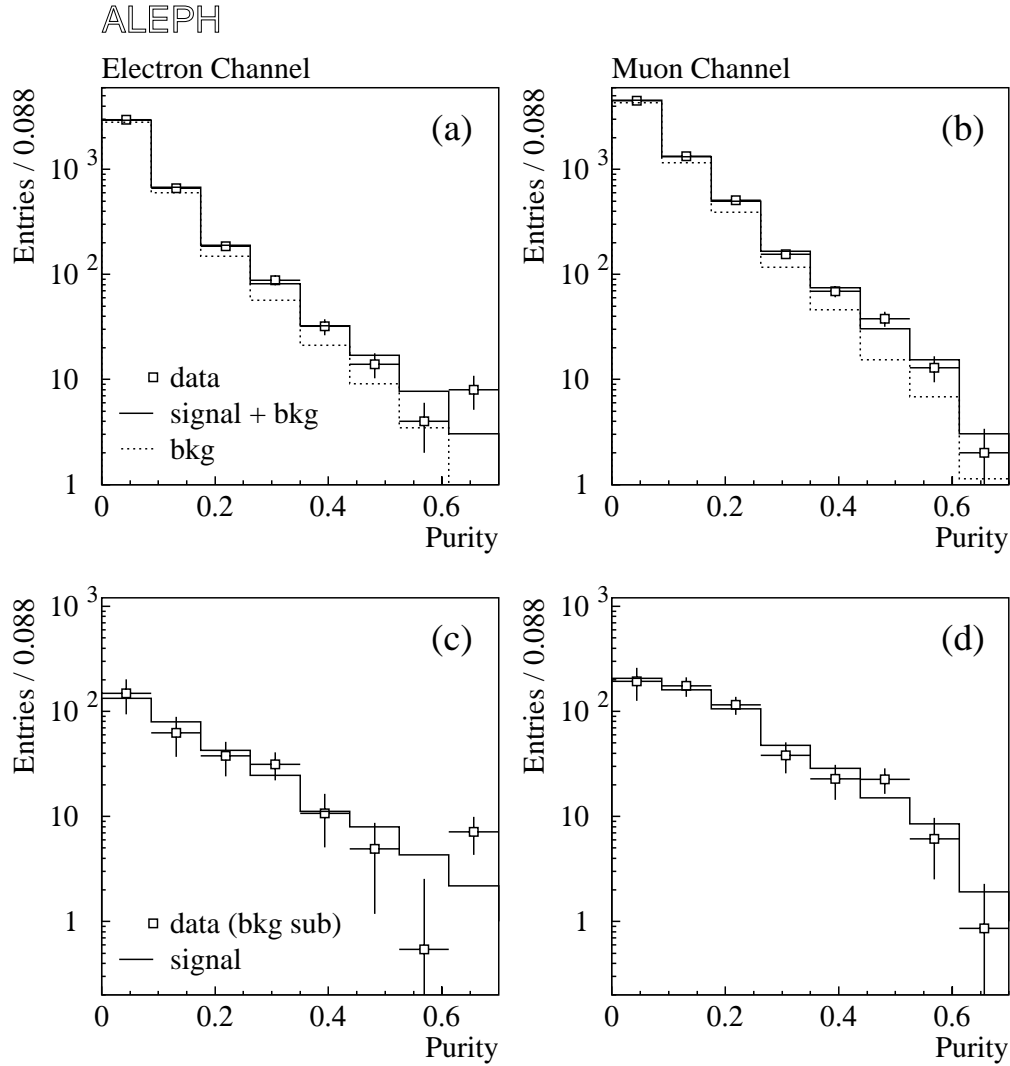
Figure 5: Distributions of purity P, in the (a) electron channel and (b) muon channel of the $D_s \to \tau\nu$ analysis. The data are shown by the squares with error bars. The histograms show the Monte Carlo distributions for the background (dotted) and for the signal plus background (solid). The Monte Carlo histograms are normalized according to the results of the fits to the data. The plots in (c) and (d) show the same distributions after subtraction of the fitted backgrounds; the squares are the data and the histograms are the Monte Carlo signal distributions. The error bars in all four plots reflect the statistical errors in the data.

Table 3: Relative normalizations of the contributions to the signal in the $D_s \to \mu\nu$ analysis.

Source	Fraction (%)
$c\bar{c} \to D_s \to \tau\nu$	49.6
$c\bar{c} \to D_s \to \mu\nu$	26.7
$b\bar{b} \to D_s \to \tau\nu$	12.6
$b\bar{b} \to D_s \to \mu\nu$	3.5
$c\bar{c} \to D^+ \to \tau\nu$	2.2
$c\bar{c} \to D^+ \to \mu\nu$	4.3
$b\bar{b} \to D^+ \to \tau\nu$	0.6
$b\bar{b} \to D^+ \to \mu\nu$	0.5
Total	100.0

c-tag neural network outputs. The U_b versus U_c distributions for signal and background events are shown in Fig. 6.

4.3 Results

The numbers of signal and background events are extracted from the data by means of a maximum likelihood fit to the $(U_c, U_b, M_{\mu\nu})$ distribution, where $M_{\mu\nu}$ is the invariant mass of the D_s candidate after the kinematic fit. The three-dimensional region $-0.6 < U_c < 1.0$, $-0.8 < U_b < 1.4$, and $M_{\mu\nu} < 5\,\mathrm{GeV}/c^2$ is divided into $6 \times 6 \times 11$ bins in the fit. The fitting functions are constructed from simulated events and a procedure is applied to smooth the distributions to reduce the bias that results from limited Monte Carlo statistics near the edges of the space.

As in the $D_s \to \tau\nu$ analysis, the signal component consists of eight contributions from D_s and D^+ decays to $\tau\nu$ and $\mu\nu$ in $c\bar{c}$ and $b\bar{b}$ events; the relative normalizations of these contributions are again fixed according to the Standard Model expectations (Table 3). Although the $\mu\nu$ invariant mass provides some separation between $D_s \to \mu\nu$ decays and the backgrounds, the $D_s \to \mu\nu$ decay mode comprises only 30% of the signal and cannot be clearly isolated in a fit to the $(U_c, U_b, M_{\mu\nu})$ distribution. With the Standard Model constraint $B(D_s \to \mu\nu)/B(D_s \to \tau\nu) = 0.103$ imposed in the fit, this analysis nevertheless yields additional information on f_{D_s}. (Fits in which this constraint is not imposed are described in Section 5.3.)

The fitted numbers of events are 553±93 signal events, 166±47 uds background events, 1251 ± 71 $c\bar{c}$ background events, and 1291 ± 62 $b\bar{b}$ background events. Figure 7 shows the fit projection on the $M_{\mu\nu}$ axis. After correction for a bias of +8.2% in the smoothing and fitting procedure, the fit result corresponds to $B(D_s \to \mu\nu) = [0.68 \pm 0.11(\mathrm{stat})]\%$. The goodness of fit is characterized by a confidence level of 69%.

The purity distribution from the $D_s \to \mu\nu$ analysis is shown in Fig. 8. The purity is defined as in Section 3.3, except in this case the signal and background distributions S and B are binned functions of U_c, U_b, and $M_{\mu\nu}$. Again the signal and background events have distinct distributions, and the shape of the background-subtracted data distribution agrees with that of the simulated signal.

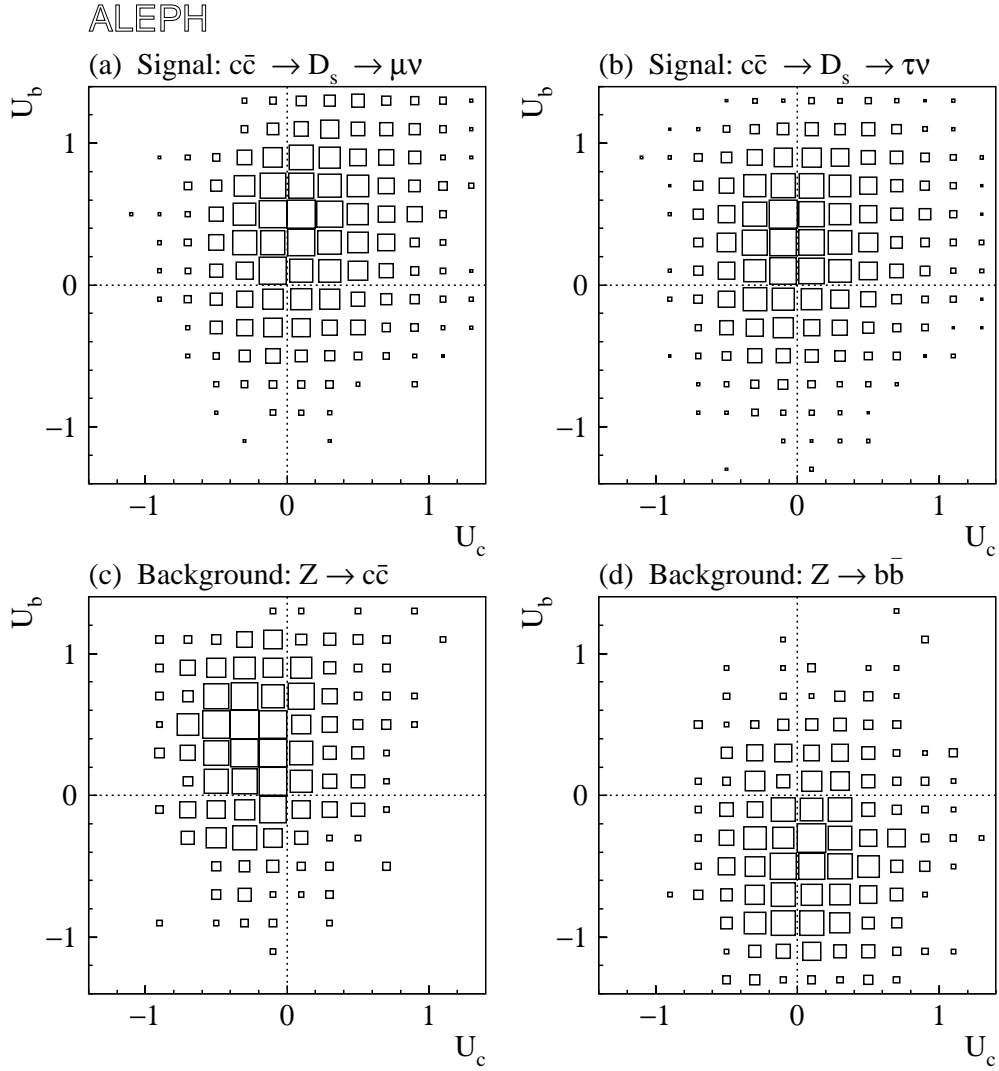Figure 6: Monte Carlo U_b versus U_c distributions in the $D_s \to \mu\nu$ analysis, after all cuts: (a) signal, $c\bar{c} \to D_s \to \mu\nu$; (b) $c\bar{c} \to D_s \to \tau\nu$, which is also included in the signal component of the fitting function; (c) $c\bar{c}$ background; (d) $b\bar{b}$ background. The distributions are shown with arbitrary normalizations.

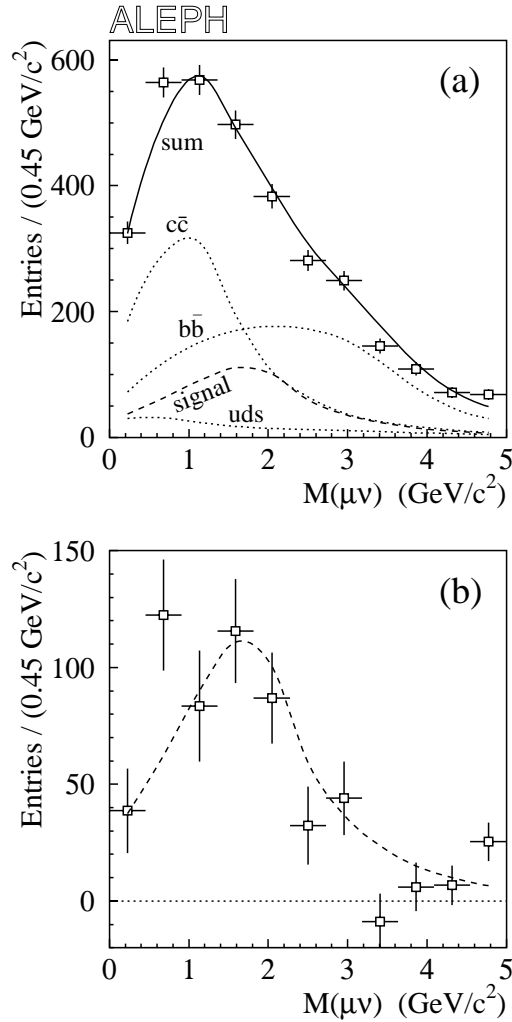Figure 7: (a) $M_{\mu\nu}$ projection of the fit to the data in the $D_s \rightarrow \mu\nu$ analysis. The data are shown by the squares with error bars. The solid curve is the fitted distribution. The dashed curve shows the signal contribution, while the dotted curves indicate the three background contributions. The data and fitted signal distributions are shown in (b), after subtraction of the fitted backgrounds.

14
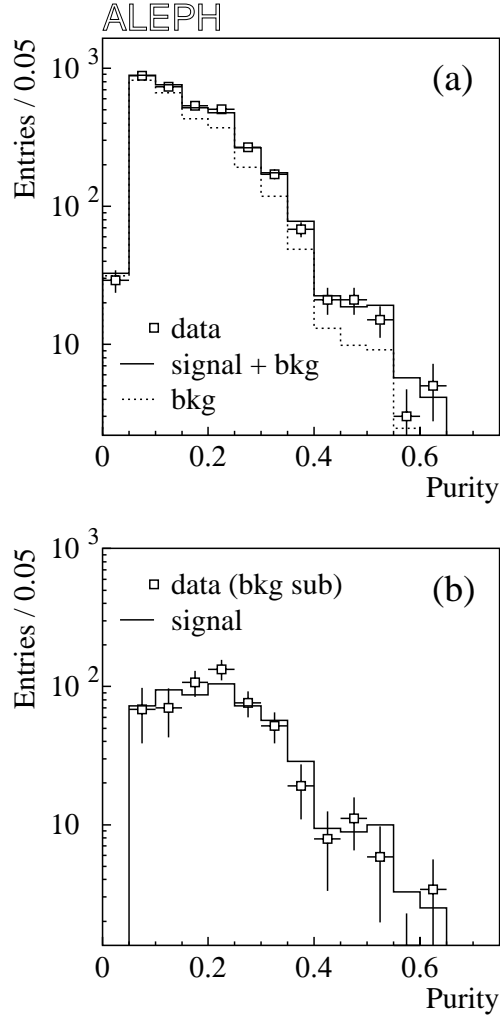
Figure 8: (a) Distribution of purity P in the $D_s \to \mu\nu$ analysis. The data are shown by the squares with error bars. The histograms show the Monte Carlo distributions for the background (dotted) and for the signal plus background (solid). The Monte Carlo histograms are normalized according to the results of the fit to the data. (b) Purity distribution after subtraction of the fitted backgrounds; the squares are the data and the histogram is the Monte Carlo signal distribution. The errors in both plots reflect the statistical errors in the data.

Table 4: Relative systematic uncertainties on $B(\mathrm{D_s} \to l\nu)$.

Source	Uncertainty (%)		
	$\mathrm{D_s} \to \tau\nu$ (e)	$\mathrm{D_s} \to \tau\nu$ (μ)	$\mathrm{D_s} \to \mu\nu$
Charm hadron production	27.0	22.8	19.6
c fragmentation	16.7	14.8	12.1
b fragmentation	9.0	5.9	4.1
Lepton spectra in b and c decays	5.5	3.6	3.1
Lepton rates in $\mathrm{b\bar{b}}$ events	0.3	0.1	1.7
Detector resolution	13.6	12.7	4.0
Monte Carlo statistics	7.2	6.0	8.8
Bias in fitting procedure	—	—	4.1
$\mathrm{D^+} \to \bar{\mathrm{K}}^0\mu^+\nu$ form factor	0.5	0.5	1.5
$f_{\mathrm{D_s}}/f_{\mathrm{D}}$	0.2	0.7	1.4
Total	36.8	31.4	26.0

5 Systematic errors

5.1 Evaluation of systematic uncertainties

In both analyses, the shapes of the signal and background fitting functions are taken from simulated events. The physics parameters that can affect these shapes are taken into account in the systematic uncertainties on the branching fractions.

The sources of systematic error are summarized in Table 4. The magnitudes of the systematic errors are estimated by measuring the branching fractions from a Monte Carlo sample, reweighting the Monte Carlo events to simulate a variation in a parameter, then measuring the branching fractions again. In each case the quoted systematic uncertainty is taken to be the quadratic sum of the observed shift and the statistical uncertainty on the shift.

The uncertainties on the production rates of $\mathrm{D^+}$, $\mathrm{D^0}$, $\mathrm{D_s}$, and charm baryons from [13, 14] are taken into account, including correlations. The $\mathrm{D_s}$ production rates have large uncertainties due mainly to the large uncertainty on the absolute scale of branching fractions for hadronic $\mathrm{D_s}$ decays; these parameters give the largest contributions to the systematic error on the leptonic branching fractions because they directly govern the number of produced $\mathrm{D_s}$ mesons in the data sample.

The Monte Carlo events are weighted to match the mean scaled energies $\langle x_E(\mathrm{c}) \rangle = 0.484 \pm 0.008$ and $\langle x_E(\mathrm{b}) \rangle = 0.702 \pm 0.008$ of charm and b hadrons given in [20]; the uncertainties on those fragmentation parameters are propagated to the leptonic branching fractions.

The shapes of the lepton energy spectra in b and c decays are varied according to the prescription given in [21]. The $\mathrm{b} \to l$ and $\mathrm{b} \to \mathrm{c} \to \bar{l}$ fractions and uncertainties are taken from [13].

The detector resolution on missing energy and momentum is dominated by the errors on neutral particle energies. The energy resolutions for neutral energy flow particles are

studied in samples of hadronic Z decays in data and Monte Carlo. The electromagnetic and hadronic energy resolution parameters for each sample are estimated by means of a global fit in which the total energy in each event is constrained to $\sqrt{s}$ and the total momentum is constrained to zero. Although the four-momentum carried away by neutrinos and objects at low angles is not taken into account in this procedure, a useful comparison of the energy resolutions in data and Monte Carlo can nevertheless be made. A discrepancy of less than 4% in the neutral particle energy resolution is observed, and the effect on the branching fractions is estimated by further smearing the neutral energies in the Monte Carlo events that are used to build the fitting functions.

The Monte Carlo statistical uncertainty is estimated by generating many toy Monte Carlo samples, using the fitting functions obtained from the full simulation as the parent distributions. This procedure reveals a +8.2% bias in the smoothing and fitting procedure in the $D_s \to \mu\nu$ analysis, and a systematic uncertainty equal to half the bias is assigned. As a cross check, a fit to the data in this channel is also performed with an algorithm in which the statistical fluctuations in the Monte Carlo distributions are taken into account [22]; the fitted number of signal events is within 2% of that obtained with the standard program, after bias corrections.

Other small effects considered are the form factor in $D^+ \to \bar{K}^0 \mu^+ \nu$ decays [23] (an important source of background) and the ratio of decay constants f_{D_s}/f_D from [15].

5.2   Cross check with $D_s \to \phi\pi$ decays

A study of $D_s \to \phi\pi$ decays is performed as a cross check of the signal efficiencies in the $D_s \to l\nu$ analyses. Candidate $D_s \to \phi\pi$ decays with $\phi \to K^+ K^-$ are first selected from the full $e^+e^- \to q\bar{q}$ sample. The dE/dx measurements in the TPC are used to discriminate between pions and kaons. Cuts are also applied on the kaon and pion momenta, the $K^+ K^-$ invariant mass, and the decay angle of the ϕ. The same selection is applied to simulated $q\bar{q}$ events containing $D_s \to \phi\pi$ decays.

The $KK\pi$ candidates are divided into seven bins of $x_E = E_{KK\pi}/E_{\text{beam}}$, from 0.3 to 1. The number of D_s mesons in each x_E bin in the data is evaluated by means of a fit to the reconstructed $KK\pi$ invariant mass distribution for the candidates in that bin. In this fit the signal is described as the sum of two Gaussian functions, and a second pair of Gaussians is included for the $D^+ \to \phi\pi$ contribution; a polynomial function is used for the background.

In order to measure the efficiencies of the $D_s \to l\nu$ selections, the pion in each $KK\pi$ combination is treated as the lepton candidate; the kaons are removed from the event and correspond to the missing neutrino(s). After the selection cuts are made, the number of D_s mesons in each x_E bin is again extracted from the $KK\pi$ invariant mass distribution. The selection efficiency in each bin is then evaluated in data and Monte Carlo. Some cuts, most notably the lepton identification cuts, cannot be studied with this method. The $D_s \to \tau\nu$ and $D_s \to \mu\nu$ analyses are checked separately.

The following aspects of the $D_s \to \tau\nu$ analysis are included in the $\phi\pi$ cross check: the cut on missing energy, the $b\bar{b}$ and dilepton rejection cuts, the kinematic fit, and the cut on the fitted D_s energy. With the kaon candidates excluded from the event, these operations can be accurately duplicated in the $\phi\pi$ events. The overall efficiency of these
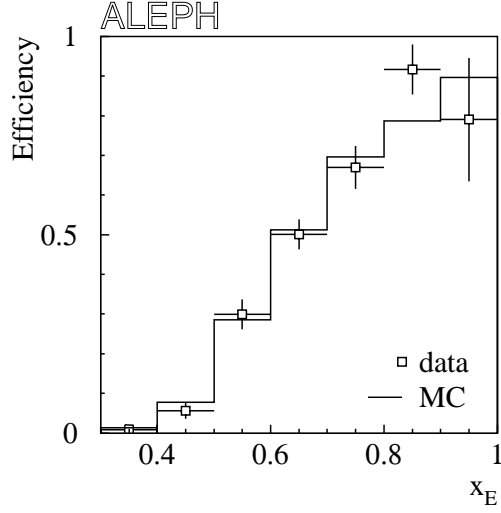
Figure 9: Efficiency versus x_E in data (squares with error bars) and Monte Carlo (histogram) for the $D_s \to \tau\nu$ selection cuts listed in the text, as measured from $D_s \to \phi\pi$ decays. The cut on the fitted D_s energy, $E_{D_s} > 22.5\,\mathrm{GeV}$, corresponds to $x_E \gtrsim 0.49$.
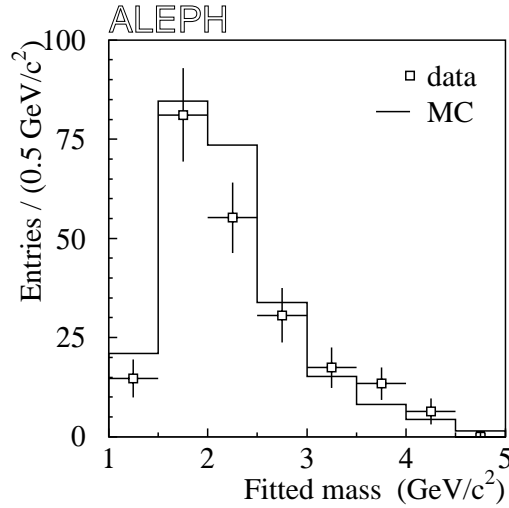
Figure 10: Background-corrected distribution of the D_s mass (calculated from the π and the missing K^+K^-) after the kinematic fit, in the $\phi\pi$ cross check of the $D_s \to \mu\nu$ analysis. The data are shown by the squares with error bars, while the histogram shows the Monte Carlo distribution. The number of D_s mesons in each mass bin in the data is obtained from a fit to the corresponding distribution of the fully reconstructed $KK\pi$ invariant mass.

Table 5: Fitted background events relative to the expected numbers in the two channels of the $D_s \rightarrow \tau\nu$ analysis and in the $D_s \rightarrow \mu\nu$ analysis. The first uncertainty given in each case is statistical and the second systematic.

| Background | Fitted / Expected Background | | |
	$D_s \rightarrow \tau\nu$ (e)	$D_s \rightarrow \tau\nu$ (μ)	$D_s \rightarrow \mu\nu$
uds	$0.81 \pm 0.40 \pm 0.58$	$1.00 \pm 0.31 \pm 0.42$	$0.84 \pm 0.22 \pm 0.17$
c$\bar{\text{c}}$	$0.92 \pm 0.04 \pm 0.06$	$0.93 \pm 0.04 \pm 0.07$	$0.96 \pm 0.05 \pm 0.08$
b$\bar{\text{b}}$	$0.92 \pm 0.05 \pm 0.05$	$1.06 \pm 0.04 \pm 0.05$	$0.98 \pm 0.05 \pm 0.06$

cuts as a function of x_E, in data and Monte Carlo, is plotted in Fig. 9. The signal efficiency (apart from lepton identification) is verified to be correctly simulated within the statistical uncertainty of the test (7% relative uncertainty).

A similar $\phi\pi$ cross check is performed for the $D_s \rightarrow \mu\nu$ analysis. The main differences with respect to the $D_s \rightarrow \tau\nu$ case are (1) the fitted primary vertex and the impact parameters of the pion (serving as the muon) are now involved in the kinematic fit, and (2) it is possible to check the resolution on the reconstructed D_s mass. For purposes of this test, the missing mass is constrained in the kinematic fit to equal the reconstructed K^+K^- invariant mass on an event-by-event basis. The measured efficiencies in data and Monte Carlo are again found to be in agreement. The distributions of reconstructed D_s mass in data and Monte Carlo are plotted in Fig. 10; the simulated resolution is found to be consistent with that observed in the data.

5.3   Additional checks

Additional checks, described in this section, are performed in order to further investigate the accuracy of the Monte Carlo simulation.

The fitted numbers of uds, c$\bar{\text{c}}$, and b$\bar{\text{b}}$ background events are compared with the Monte Carlo predictions in Table 5. The normalization of the predicted numbers is based on the total number of produced $e^+e^- \rightarrow q\bar{q}$ events in the data sample. The predictions for $D_s \rightarrow \mu\nu$ are corrected for biases in the fitting procedure. The data and Monte Carlo are in agreement. A χ^2 value is computed to characterize this agreement in the $D_s \rightarrow \mu\nu$ analysis, taking into account the correlations in the statistical and systematic errors on the normalizations of the three backgrounds. The result is $\chi^2 = 0.74$ for three degrees of freedom (CL = 87%).

The distributions of the event variables used to construct the three sets of linear discriminant variables U_c and U_b are compared in data and Monte Carlo to ensure that the simulation is reliable. The Monte Carlo plots are normalized according to the results of the fits to the data. No significant discrepancies are found.

Another cross check on the accuracy of the simulation is made by comparing the distributions of certain quantities in data and Monte Carlo in different regions of the (U_c, U_b) space. In each analysis, four disjoint regions in that space are defined with different relative abundances of the signal and the three backgrounds. The Monte Carlo normalization is again based on the results of the fits to the data. The quantities studied

19

in the $D_s \to \tau\nu$ analysis include the fitted D_s momentum, the angle between the lepton and the D_s momentum in the D_s rest frame, and b tag variables; in the $D_s \to \mu\nu$ analysis the missing energy before the kinematic fit, the $\mu\nu$ invariant mass after the kinematic fit, and the fitted proper D_s decay length were considered. The simulation is found to be consistent with the data in all cases and in all regions of the (U_c, U_b) space. This check demonstrates that the properties of the backgrounds are correctly reproduced in the Monte Carlo.

The fit to the data in the $D_s \to \mu\nu$ analysis was repeated without the Standard Model constraint on $B(D_s \to \mu\nu)/B(D_s \to \tau\nu)$. For this calculation, the signal contributions from D_s and D^+ decays to $\mu\nu$ were allowed to vary separately from the $\tau\nu$ contributions. The fitted contribution from $\mu\nu$ relative to $\tau\nu$ is found to be somewhat smaller than expected; Monte Carlo experiments show that the unconstrained fit is expected to give a $\mu\nu/\tau\nu$ ratio smaller than the observed value 5% of the time when the events are generated according to the Standard Model ratio. The fitted $\mu\nu/\tau\nu$ ratio is not sensitive to the assumed charm production rates or fragmentation parameters.

Increased sensitivity to $B(D_s \to \mu\nu)$ is achieved if the $D_s \to \mu\nu$ analysis is coupled to the statistically independent electron channel of the $D_s \to \tau\nu$ analysis. The fit described in the preceding paragraph is repeated with a modified likelihood function in which $B(D_s \to \tau\nu)$ is constrained according to the value and uncertainty obtained from the electron channel; after correction for the calculated -1% and $+14\%$ biases, respectively, the results are

$$
\begin{aligned}
B(D_s \to \mu\nu) &= (0.47 \pm 0.25)\% \\
B(D_s \to \tau\nu) &= (6.8 \pm 1.0)\% \ ,
\end{aligned}
$$

where the uncertainties are statistical only.

6   Conclusions

Leptonic decays of the D_s meson have been studied in a sample of four million hadronic Z decays. The $D_s \to \tau\nu$ analysis gives

$$
\begin{aligned}
B(D_s \to \tau\nu) &= (5.86 \pm 1.18 \pm 2.16)\% \ , && \text{(electron channel)} \\
&= (5.78 \pm 0.85 \pm 1.81)\% \ , && \text{(muon channel)}
\end{aligned}
$$

where the measured signal includes some $D_s \to \mu\nu$ and $D^+ \to l\nu$ decays. In the Standard Model, these branching fractions correspond to the following values of the decay constant f_{D_s}:

$$
\begin{aligned}
f_{D_s} &= (275 \pm 28 \pm 51)\,\text{MeV} \ , && \text{(electron channel)} \\
&= (273 \pm 20 \pm 43)\,\text{MeV} \ . && \text{(muon channel)}
\end{aligned}
$$

These results are combined, taking into account the common systematic errors [24], to obtain

$$
\begin{aligned}
B(D_s \to \tau\nu) &= (5.79 \pm 0.77 \pm 1.84)\% \\
f_{D_s} &= (273 \pm 18 \pm 43)\,\text{MeV} \ .
\end{aligned}
$$

The combination has $\chi^2 = 0.0024$ for 1 degree of freedom (CL = 96%). This measurement may be expressed as

$$f(\mathrm{c} \to \mathrm{D_s})B(\mathrm{D_s} \to \tau\nu) = (6.77 \pm 0.90 \pm 1.49) \times 10^{-3} \; ,$$

where $f(\mathrm{c} \to \mathrm{D_s})$ is the $\mathrm{D_s}$ production rate per hemisphere in $\mathrm{Z} \to \mathrm{c\bar{c}}$ events; the relative uncertainty on this product is smaller than that on $B(\mathrm{D_s} \to \tau\nu)$ due to the reduced dependence on the assumed $\mathrm{D_s}$ production rate.

The analysis optimized for $\mathrm{D_s} \to \mu\nu$ is also sensitive to $\mathrm{D_s} \to \tau\nu$ decays; a measurement of the combined signal yields

$$B(\mathrm{D_s} \to \mu\nu) = (0.68 \pm 0.11 \pm 0.18)\%$$

when the ratios of the signal components are fixed to their Standard Model values. This measurement corresponds to

$$f_{\mathrm{D_s}} = (291 \pm 25 \pm 38)\,\mathrm{MeV} \; .$$

Finally, the three $f_{\mathrm{D_s}}$ measurements (two from $\tau\nu$ and one from $\mu\nu$) are combined. The correlation coefficient $k = +0.43 \pm 0.34$ of the statistical errors in the $\mathrm{D_s} \to \mu\nu$ analysis and the muon channel of the $\mathrm{D_s} \to \tau\nu$ analysis is evaluated by dividing the data into ten subsamples. The correlations between the systematic errors are also taken into account. The combined decay constant is

$$f_{\mathrm{D_s}} = (285 \pm 19 \pm 40)\,\mathrm{MeV}$$

with $\chi^2 = 0.51$ for 2 degrees of freedom (CL = 78%).

This result is consistent with recent measurements [16, 25, 26] and with the lattice QCD prediction, $f_{\mathrm{D_s}} = 255 \pm 30\,\mathrm{MeV}$ [1].

Acknowledgements

References

[1] C. Bernard, "Heavy Quark Physics on the Lattice", Nucl. Phys. Proc. Suppl. **94** (2001) 159, `hep-lat/0011064`.

[2] G. Burdman, T. Goldman, and D. Wyler, "Radiative Leptonic Decays of Heavy Mesons", Phys. Rev. **D51** (1995) 111.

[3] D. Atwood, G. Eilam, and A. Soni, "Pure Leptonic Radiative Decays $\mathrm{B^{\pm}}, \mathrm{D_s} \to l\nu\gamma$ and the Annihilation Graph", Mod. Phys. Lett. **A11** (1996) 1061.

[4] ALEPH Collaboration, "ALEPH: a Detector for Electron-positron Annihilations at LEP", Nucl. Instrum. Methods **A294** (1990) 121.

[5] B. Mours et al., "The Design, Construction and Performance of the ALEPH Silicon Vertex Detector", Nucl. Instrum. Methods **A379** (1996) 101.

[6] ALEPH Collaboration, "Performance of the ALEPH Detector at LEP", Nucl. Instrum. Methods **A360** (1995) 481.

[7] ALEPH Collaboration, "A Study of the Decay Width Difference in the B_s^0-$\bar{B}_s^0$ System Using $\phi\phi$ Correlations", Phys. Lett. **B486** (2000) 286.

[8] L. He, "A Measurement of the Branching Fraction of the D_s Meson Decay into a Tau and a Neutrino", Ph.D. thesis, University of Washington, 2000.

[9] ALEPH Collaboration, "Measurement of the Z Resonance Parameters at LEP", Eur. Phys. J. **C14** (2000) 1.

[10] ALEPH Collaboration, "Heavy Quark Tagging with Leptons in the ALEPH Detector", Nucl. Instrum. Methods **A346** (1994) 461.

[11] ALEPH Collaboration, "Measurement of the B_s^0 Lifetime", Phys. Lett. **B322** (1994) 275.

[12] ALEPH Collaboration, "A Precise Measurement of $\Gamma(Z \to b\bar{b})/\Gamma(Z \to \text{hadrons})$", Phys. Lett. **B313** (1993) 535.

[13] The LEP Collaborations, the LEP Electroweak Working Group, and the SLD Heavy Flavor and Electroweak Groups, "A Combination of Preliminary Electroweak Measurements and Constraints on the Standard Model", preprint CERN-EP/2000-016.

[14] ALEPH Collaboration, "Charm Counting in b Decays", Phys. Lett. **B388** (1996) 648.

[15] T. Draper, "Status of Heavy Quark Physics on the Lattice", Nucl. Phys. Proc. Suppl. **73** (1999) 43, `hep-lat/9810065`.

[16] D.E. Groom et al. (Particle Data Group), "Review of Particle Physics", Eur. Phys. J. **C15** (2000) 1.

[17] T. Sjöstrand, "High-energy Physics Event Generation with PYTHIA 5.7 and JETSET 7.4", Comp. Phys. Commun. **82** (1994) 74.

[18] ALEPH Collaboration, "Heavy Flavor Production and Decay with Prompt Leptons in the ALEPH Detector", Z. Phys. **C62** (1994) 179; "Studies of Quantum Chromodynamics with the ALEPH Detector", Phys. Rep. **294** (1998) 1.

[19] J. Putz, "A Measurement of the Branching Fraction of the D_s Meson to a Muon and a Neutrino", Ph.D. thesis, University of Washington, 1999.

[20] The LEP Heavy Flavour Working Group, "Input Parameters for the LEP/SLD Electroweak Heavy Flavour Results for Summer 1998 Conferences", LEPHF/98-01 (1998).

[21] The LEP Heavy Flavour Working Group, "A Consistent Treatment of Systematic Errors for LEP Electroweak Heavy Flavour Analyses", LEPHF 94-001 (1994).

[22] `HBOOK` routine `hmcmll`; R. Barlow and C. Beeston, "Fitting Using Finite Monte Carlo Samples", Comp. Phys. Commun. **77** (1993) 219.

[23] CLEO Collaboration, "Measurement of Exclusive Semileptonic Decays of D Mesons", Phys. Lett. **B317** (1993) 647.

[24] L. Lyons, D. Gibaut, and P. Clifford, "How to Combine Correlated Estimates of a Single Physical Quantity", Nucl. Instrum. Methods **A270** (1988) 110.

[25] BEATRICE Collaboration, "Measurement of the $D_s \to \mu\nu_\mu$ Branching Fraction and of the D_s Decay Constant", Phys. Lett. **B478** (2000) 31.

[26] OPAL Collaboration, "Measurement of the Branching Ratio for $D_s^- \to \tau^- \bar{\nu}_\tau$ Decays", Phys. Lett. **B516** (2001) 236, `hep-ex/0103012`.